ELSEVIER

Chemical Geology 210 (2004) 91–111

CHEMICAL GEOLOGY
INCLUDING
ISOTOPE GEOSCIENCE

www.elsevier.com/locate/chemgeo

Conditions of pocket formation in the Oktyabrskaya tourmaline-rich gem pegmatite (the Malkhan field, Central Transbaikalia, Russia)

Igor S. Peretyazhko[a,*], Victor Ye. Zagorsky[a], Sergey Z. Smirnov[b], Mikhail Y. Mikhailov[b]

[a] *Vinogradov Institute of Geochemistry, Siberian Branch, Russian Academy of Science, Favorsky St. 1a, Irkutsk, 664033, Russia*
[b] *Institute of Mineralogy and Petrography, Siberian Branch, Russian Academy of Science, prosp. Akad. Koptyuga 3, Novosibirsk, 630090, Russia*

Abstract

Coexisting melt (MI), fluid-melt (FMI) and fluid (FI) inclusions in quartz from the Oktaybrskaya pegmatite, central Transbaikalia, have been studied and the thermodynamic modeling of PVTX-properties of aqueous orthoboric-acid fluids has been carried out to define the conditions of pocket formation. At room temperature, FMI in early pocket quartz and in quartz from the coarse-grained quartz–oligoclase host pegmatite contain crystalline aggregates and an orthoboric-acid fluid. The portion of FMI in inclusion assemblages decreases and the volume of fluid in inclusions increases from the early to the late growth zones in the pocket quartz. No FMI have been found in the late growth zones. Significant variations of solid/fluid ratios in the neighboring FMI result from heterogeneous entrapment of coexisting melts and fluids by a host mineral. Raman spectroscopy, SEM EDS and EMPA indicate that the crystalline aggregates in FMI are dominated by mica minerals of the boron-rich muscovite–nanpingite $CsAl_2[AlSi_3O_{10}](OH,F)_2$ series as well as lepidolite. Topaz, quartz, potassium feldspar and several unidentified minerals occur in much lower amounts. Fluid isolations in FMI and FI have similar total salinity (4–8 wt.% NaCl eq.) and H_3BO_3 contents (12–16 wt.%). The melt inclusions in host-pegmatite quartz homogenize at 570–600 °C. The silicate crystalline aggregates in large inclusions in pocket quartz completely melt at 615 °C. However, even after those inclusions were significantly overheated at 650 ± 10 °C and 2.5 kbar during 24 h they remained non-homogeneous and displayed two types: (i) glass + unmelted crystals and (ii) fluid + glass. The FMI glasses contain 1.94–2.73 wt.% F, 2.51 wt.% B_2O_3, 3.64–5.20 wt.% Cs_2O, 0.54 wt.% Li_2O, 0.57 wt.% Ta_2O_5, 0.10 wt.% Nb_2O_5, 0.12 wt.% BeO. The H_2O content of the glass could exceed 12 wt.%. Such compositions suggest that the residual melts of the latest magmatic stage were strongly enriched in H_2O, B, F, Cs and contained elevated concentrations of Li, Be, Ta, and Nb. FMI microthermometry showed that those melts could have crystallized at 615–550 °C.

Crystallization of quartz–feldspar pegmatite matrix leads to the formation of H_2O-, B- and F-enriched residual melts and associated fluids (prototypes of pockets). Fluids of different compositions and residual melts of different liquidus–solidus *P–T*-conditions would form pockets with various internal fluid pressures. During crystallization, those melts release more aqueous fluids resulting in a further increase of the fluid pressure in pockets. A significant overpressure and a possible pressure gradient between the neighboring pockets would induce fracturing of pockets and ‘‘fluid explosions’’. The fracturing commonly results in the crushing of pocket walls, formation of new fractures connecting adjacent pockets, heterogenization and mixing of pocket

* Corresponding author. Tel.: +7-3952-425936; fax: +7-3952-427050.
E-mail address: pgmigor@igc.irk.ru (I.S. Peretyazhko).

0009-2541/$ - see front matter
doi:10.1016/j.chemgeo.2004.06.005

fluids. Such newly formed fluids would interact with a primary pegmatite matrix along the fractures and cause autometasomatic alteration, recrystallization, leaching and formation of "primary–secondary" pockets.

Keywords: Miarolitic pegmatites; Pocket; Residual melts; Boric acid solutions; Melt and fluid inclusions; Sassolite; Fluid pressure; Isochores

1. Introduction

Pegmatites with mineralized *miarolitic cavities* (e.g. pockets, vugs, miaroles) represent a valuable source of gems, piezoelectric materials and collection specimens. Since the middle of the past century, all miarolitic pegmatites have been traditionally regarded as a specific low-pressure shallow-seated category, which has been opposed to rare-metal, muscovite and other pegmatites of higher-pressure and much deeper-seated categories (Fersman, 1960; Ginzburg and Rodionov, 1960; Černý, 1992; etc.). In the modern classification by Zagorsky et al. (1999a,b; 2003), which is used hereinafter, the shallow-seated rock crystal, i.e. quartz (± fluorite) and sub-rare-metal[1] pegmatites with gem-quality topaz, beryl and tourmaline are considered a separate crystal-bearing category. However, the existing data indicate that the pockets are not related to shallow pegmatites only. Residual miarolitic cavities have also been found in deeper rare-metal, rare-metal-muscovite and even muscovite pegmatites. Therefore, cavity-bearing pegmatites represent a special *miarolitic facies*, which may be formed within a rather wide range of pressures in pegmatites of various categories (Zagorsky and Shmakin, 1987, 1997; Zagorsky et al., 1999a,b, 2003). Thus, it became vital to revise the current view on the conditions of pocket formation and on the position of miarolitic pegmatites in the classification of granitic pegmatites, as was also proposed by Černý (2000).

Pressure is an important, but not the only, parameter governing pocket formation. London (1986) reported similar P–T-conditions for crystallization of non-miarolitic (Tanco, Canada) and miarolitic (Kulam, Afghanistan and San Diego County, CA) rare-metal pegmatites. He related the formation of pockets in such pegmatites to massive tourmaline crystallization from residual melts, which resulted in a release of an aqueous fluid due to boron removal and decrease of water solubility in the melt. In our opinion, this effect is overestimated, as the volume and abundance of miarolitic cavities do not correlate with amounts of tourmaline in adjacent pegmatite assemblages (Zagorsky et al., 1999b). Besides, the formation of pockets seems to depend on the total amount and mass ratios of volatile components in pegmatitic melts. Drastic variability of compositions of miarolitic fluids can be seen even within one category of crystal-bearing pegmatites. For example, boric acid is one of the major solutes of miarolitic fluids in sub-rare-metal and rare-metal pegmatites (Peretyazhko et al., 1999, 2000; Smirnov et al., 2000), whereas chlorides and probably fluorine dominate in aqueous and aqueous-carbon-dioxide fluids of topaz–beryl and rock crystal (± fluorite) pegmatites. The behavior of volatiles is greatly important at the transition from magmatic to hydrothermal crystallization. The pegmatitic system at this stage may consist of several liquids–aqueous fluids and/or silica-based melts with extraordinary concentrations of H_2O, B, F, P, and such economically important metals as Li, Be, Ta, Nb, Sn and Cs (Kovalenko et al., 1996; Veksler et al., 2002; Peretyazhko et al., 2002a,b; Smirnov et al., 2003; Thomas et al., 2000, 2003).

The above brief review displays the versatility of the available data that cast light on the miarolitic stage of pegmatite formation. However, data on specific conditions of pocket formation are still scarce. This paper represents the first data on P–T conditions, composition and aggregation of mineral-forming media at the pocket formation in the boron-rich Oktyabrskaya gem pegmatite (Central Transbaikalia, Russia), belonging to the tourmaline-rich sub-rare-metal pegmatites of the crystal-bearing category (Zagorsky et al., 1999a,b, 2003).

[1] The sub-rare-metal group in the crystal-bearing category includes pegmatites with typical rare-metal minerals, such as beryl, lepidolite, elbaite, petalite, etc., but nevertheless the contents of rare elements—Li, Be, Cs, Ta, Nb, Sn—are much lower than those in rare metal pegmatites.

2. Geological setting and description of the Oktyabrskaya pegmatite

The Malkhan pegmatite field and its related gem tourmaline deposit are situated at the north slope of the Malkhan ridge, at the right bank of the Chikoy midstream, about 200 km southeast of Ulan-Ude (Fig. 1). The detailed study of geology, internal structure, mineralogy and geochemistry of Malkhan pegmatites has been performed by Zagorsky and Peretyazhko and reported in Zagorsky and Peretyazhko (1992a) and Zagorsky et al. (1999b). The Malkhan field is bounded by the Chikoy deep fault system from the south, which separates the Caledonian foldbelt in the north and Hercynian and Kimmerian foldbelts in the south. The field is confined to the sag of the roof of Mesozoic porphyritic biotite granites and biotite and two-mica leucogranites. The pegmatites are hosted by early Paleozoic [Pz_1] primary intrusive rocks of the Malkhan complex, which were metamorphosed in amphibolite facies conditions. This field comprises several hundred of lens- and plate-shaped pegmatite bodies. About 40 pegmatites contain pockets with gem mineralization, but only a half of them are of commercial interest. The Oktyabrskaya pegmatite is a gently dipping lenticular body 250 m long and up to 7–8 m thick hosted by metadiorites. It is a typical, highly productive gem tourmaline pegmatite. The pegmatite consists of graphic, sub-graphic, and to a lesser extent pegmatoidal quartz–oligoclase and quartz–potassium feldspar varieties with minor schorl, biotite and almandine–spessartine garnet. Subordinate are small blocky feldspar and quartz, as well as near-pocket quartz–tourmaline–lepidolite–albite assemblages. Typically quartz–oligoclase and quartz–potassium feldspar varieties irregularly alternate irrespective of position in the pegmatite. However, statistically oligoclase dominates the external zones of pegmatites, while the potassium–feldspar content increases in the internal zones. Miarolitic cavities can be hosted by any variety and locate in almost any part of the body, even near its contacts. The thinnest outermost parts of the body are the only parts that are devoid of pockets. The volume of the pockets varies from cubic centimeters to cubic meters. The main minerals in the pockets are quartz, potassium feldspar, cleavelandite, lepidolite, colored tourmaline, danburite and hambergite.

The largest pockets (>0.5 m across) in the Malkhan pegmatites reveal decrepitation and fluid incursion into the fractures of the hosting quartz–feldspar pegmatite. The neighboring pockets are often interconnected via small channels and veinlets indicating an exchange of matter between them. This makes the correlation between certain mineral parageneses and processes of pocket formation difficult. That was why we selected a small isolated isometric pocket (about 15 cm across) for our study. This pocket shows no rupturing and overprinting of late processes. It has typical mineral composition, morphology, and relations to early quartz–feldspar assemblages.

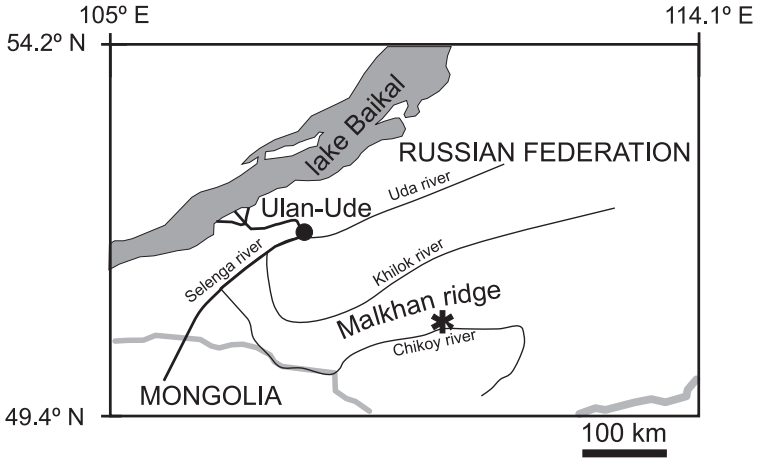

Fig. 1. Location of the study area. Asterisk shows the location of Malkhan pegmatite field. Oktyabrskaya pegmatite mine is located at 50°39′ N, 109°53′ E.

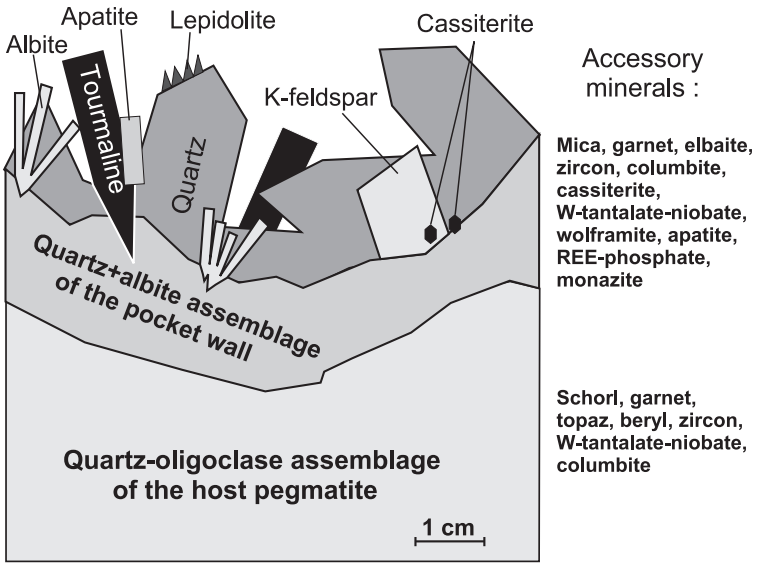

Fig. 2. Schematic cross section through the studied miarolitic cavity.

Fig. 2 shows the structure and mineral parageneses of the pocket under investigation. The pocket is hosted by medium-grained, quartz–oligoclase pegmatite with minor red almandine–spessartine, schorl, and accessory W-rich tantaloniobate mineral, beryl, topaz, and zircon. This pegmatite grades into a 1–2 cm thick, coarse-grained quartz–albite zone of the pocket wall that contains minor mica, almandine–spessartine garnet, and tourmaline. The tourmaline of this assemblage typically has a black schorl core, light-yellow intermediate elbaite zone and pink elbaite outer zone. Accessory topaz, zircon, cassiterite, tantaloniobates, apatite, monazite and REE-phosphate occur in the quartz–albite zone.

The outermost parts of the quartz–albite zone have an euhedral appearance and are usually referred to as a druse assemblage. The druse assemblage consists of smoky quartz crystals with radiating aggregates of white platelet cleavelandite and subordinate potassium feldspar and pink tourmaline. Black 3 by 5 mm cassiterite grains are included in the base part of one quartz crystal. The only pale blue apatite crystal (1 × 0.3 cm) was found in association with pink tourmaline (1 × 0.6 ñm) as well. The outermost faces of several quartz crystals are covered by a 2–3 mm thick crust of fine-flaked lepidolite. Tables 1a and 1b show compositions of minor and accessory minerals from the druse assemblage and the host pegmatite.

3. Experimental and analytical methods

Thick (0.3–0.5 mm) double-polished sections were made from the samples taken across all pocket assemblages and the hosting pegmatite (at about 8 cm from the pocket wall). The inclusions of mineral-forming media have been selected by means of optical microscopy. Microthermometric measurements were carried out at the Vinogradov Institute of Geochemistry (Irkutsk, Russia) and the United Institute of Geology, Geophysics and Mineralogy (UIGGM, Novosibirsk, Russia) using the heating and freezing stages constructed by Kalyuzhnyi (1958), Mikhailov and Shatsky (1975), and Simonov (1993) with precisions of: eutectic ($T_{eut.}$) of ± 1.5 °C, melting of ice (T_{ice}) and sassolite dissolution ($T_{sas.}$) of ± 0.2 °C and homogenization ($T_{hom.}$) ± 2.0 °C.

Small (1–2 μm) melt inclusions (MI) in quartz were studied by the standard quenching technique at atmospheric pressure. The section fragments were placed in a furnace with a calibrated thermocouple and heated up to a temperature of 450–650 ± 10 °C with 10 °C steps during 5–6 h. As the final temperature was reached,

the fragments were isothermally held for 3 h and then quenched in air. The experiments on the heating of large (up to 100 + μm) MI in the pocket quartz were conducted under an external water pressure in a cold seal autoclave. The fragments of the sections containing MI were placed in a 1.5 cm^3 copper ampoule together with crushed quartz to avoid their significant dissolution. The plates were heated up to temperatures of 500, 550, 580, 600 and 650 °C (± 10–15 °C) during 1–2 h and then held at the respective final temperatures for 14–24 h. After the isothermal exposure, the autoclave was rapidly quenched in water. The volume of water in autoclave was calculated to reach 2–2.5 kbar at the final temperature.

Daughter minerals of the MI and FI were identified by means of Raman spectroscopy. For this purpose TRIPLIMATE SPEX (Institute of Inorganic Chemistry SB RAS, Novosibirsk, Russia) and X–Y Dilor (Institute of Mineralogy and Petrography SB RAS, Novosibirsk, Russia) multichannel Raman spectrometers, equipped with Peltier-cooled CCD detectors were used. The samples were excited using 514 and 498-nm lines of Ar^+laser with the power ranging from 0.3 to 1.5 W. Fluid inclusions (FI) and MI in quartz from the quartz–oligoclase pegmatite surrounding the miarolitic cavity, and from the pocket walls contain daughter crystals of orthoboric acid–sassolite (H_3BO_3). Sassolite was positively identified by Raman spectroscopy. The Raman spectrum of sassolite is marked by a strong line at 880 cm^{-1} and a less intense line at about 500 cm^{-1}, which correspond to the B–O symmetric stretching in the BO_3 planar trigonal group. The problems of identification of sassolite and dissolved H_3BO_3 in fluid inclusions were previously discussed in details by (Smirnov et al., 2000; Thomas et al., 2000; Thomas, 2002).

To study the composition of melt and crystalline inclusions in quartz, the section fragments were placed in epoxy resin and then polished until the selected crystal inclusions or MI were exposed. The exposed daughter minerals of MI, glasses of re-melted inclusions and crystal inclusions were first studied with a LEO 1430VP scanning electron microscope (SEM) equipped with an EDS system by Oxford Instruments (United Institute of Geology, Geophysics and Mineralogy SB RAS, Novosibirsk, Russia) and by a Camebax-Micro microprobe (EMPA) (United Institute of Geology, Geophysics and Mineralogy SB RAS), operating at 15 kV accelerating voltage and 10–80 nA beam current and 3–20 μm beam diameter. The EMPA analysis of remelted MI glasses was performed with a special adjustment to avoid Na-loss, which will be described below. The following standards were used for calibration: albite for Si and Na, orthoclase for K and Al, synthetic F-phlogopite for F, F-apatite for P, Cl-apatite for Cl, diopside for Ca and Mg, synthetic rubidium wolframate for Rb, cesium molybdate for Cs, ilmenite for Ti, lithium niobate for Nb, Ta_2O_5 for Ta, synthetic ferberite for W, metallic Sc for Sc, and synthetic SnO_2 for Sn. The ZAF correction was applied for matrix effects. The accuracy was within 10 relative %. Ta, Nb, Be, Li, H_2O and B contents of the re-melted inclusion glasses and selected daughter minerals were analyzed at the Institute of Microelectronics and Informatics RAS (Yaroslavl, Russia) by secondary-ion mass-spectrometry (SIMS) using a Cameca IMS-4f ion microprobe, with well-defined synthetic glasses serving as standards. The applied method was essentially the same as reported by Sobolev (1996). The primary O^- ion beam was about 25 μm and we selected inclusions for analysis accordingly. The energy filtering technique was applied and ions with 50 eV energy offset were used for analysis. An average of 5 analyses of each spot was used for calculation of element contents. Trace-element and H^+contents were measured separately. H_2O content was calculated from H^+concentration. The sample was subjected to 2–3 days evacuation prior to H^+analysis to avoid contamination by atmospheric water. Special attention was paid to migration of highly volatile $H^+$and B during SIMS analysis. $^1H/^{30}Si$ ratios remained almost constant in the course of 5 analyses of the same spot, while $^{11}B/^{30}Si$ grew slightly from 3.8×10^{-6} to 4.0×10^{-6}. Identification of other minerals from the pocket assemblages and the surrounding pegmatite was performed by optical microscopy, EMPA, SEM EDS, and X-ray diffraction analysis.

4. Calculation of H_3BO_3 content and salinity of FI and MI fluids

A special technique for determination of the H_3BO_3 content and salinity of homogeneous aqueous fluids in inclusions was developed on the basis of the temperatures of sassolite dissolution and ice melting in the

$NaCl-H_3BO_3-H_2O$ system. This system was selected on the assumption that dissolved anions are compensated primarily by Na^+. This is a conventional approach in fluid inclusion study because, at a salt concentration of less than ca 20 wt.%, the total salinity of inclusions can be estimated through equivalent amounts of NaCl (Roedder, 1984). The previous studies of similar pegmatite assemblages indicated that pegmatitic fluids contain various alkaline–metal chlorides (Smirnov et al., 2000), however we will show below that the $NaCl-H_3BO_3-H_2O$ system is appropriate for determination of inclusion compositions. Figs. 3 and 4 illustrate the available experimental data on the joint solubility of NaCl and H_3BO_3 in aqueous solutions (Palkin and Goloschapov, 1939; Zhdanoviskii et al., 1975; Di Giacomo et al., 1993). The estimation of errors appearing if a system contains non-NaCl dissolved salts by Peretyazhko et al. (2000) showed that the errors would be within ± 1–1.5 wt.% at 10 wt.% KCl, $CaCl_2$, $MgCl_2$, LiCl, Na_2SO_4 or K_2SO_4 in the solution. A significant underestimation of H_3BO_3 content is expected for FI enriched in fluorine and sodium since boron can enter aqueous boron–fluoride complexes, e.g. BF_4^-, $BF_n(OH)_{4-n}^-$, $NaBF_4^0$, etc. This stems from the high solubility of fluoborates and strong bonding of orthoboric acid by sodium fluoride in aqueous solutions (Ryss et al., 1952; Ryss, 1956).

5. Melt and fluid inclusions

5.1. Melt and fluid inclusion petrography

Druse quartz and host pegmatite quartz contain numerous inclusions of mineral-forming media. The inclusions that are irregularly distributed within a host mineral were considered primary. We carefully

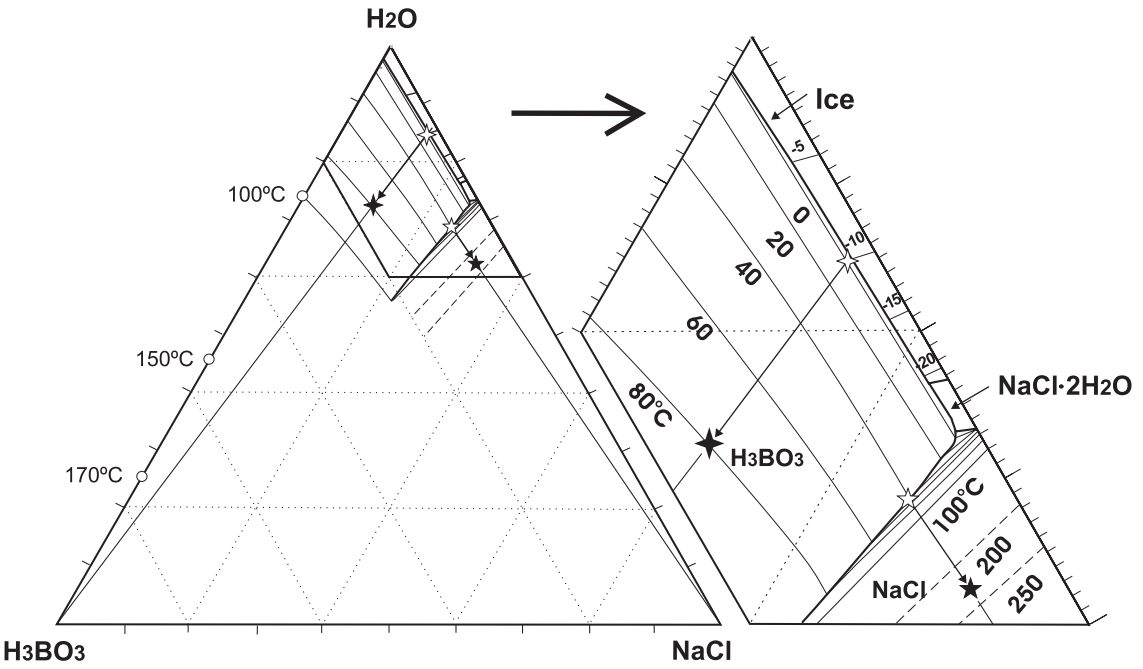

Fig. 3. Solubility diagram of $NaCl-H_3BO_3-H_2O$ system constructed from data by Palkin and Goloschapov (1939), Zhdanoviskii et al. (1975), and Di Giacomo et al. (1993). Procedure of calculation of NaCl and H_3BO_3 concentrations is shown for fluid inclusions, containing daughter sassolite (1st type, four-ray stars) and daughter sassolite + halite (2nd type, five-ray stars) crystals. The procedure begins with determination of ice melting (1st type) or sassolite dissolution (2nd type) temperatures (open stars). Once these phases disappear, the composition of solution follows the arrows up to the isotherm of last phase dissolution (sassolite in the 1st type or halite in the 2nd type inclusions). Filled stars show composition of systems where sassolite dissolves at 80 °C and halite at 230 °C. See Peretyazhko et al. (2000) and Smirnov et al. (2000) for the detailed description of calculation procedure and discussion of possible errors.

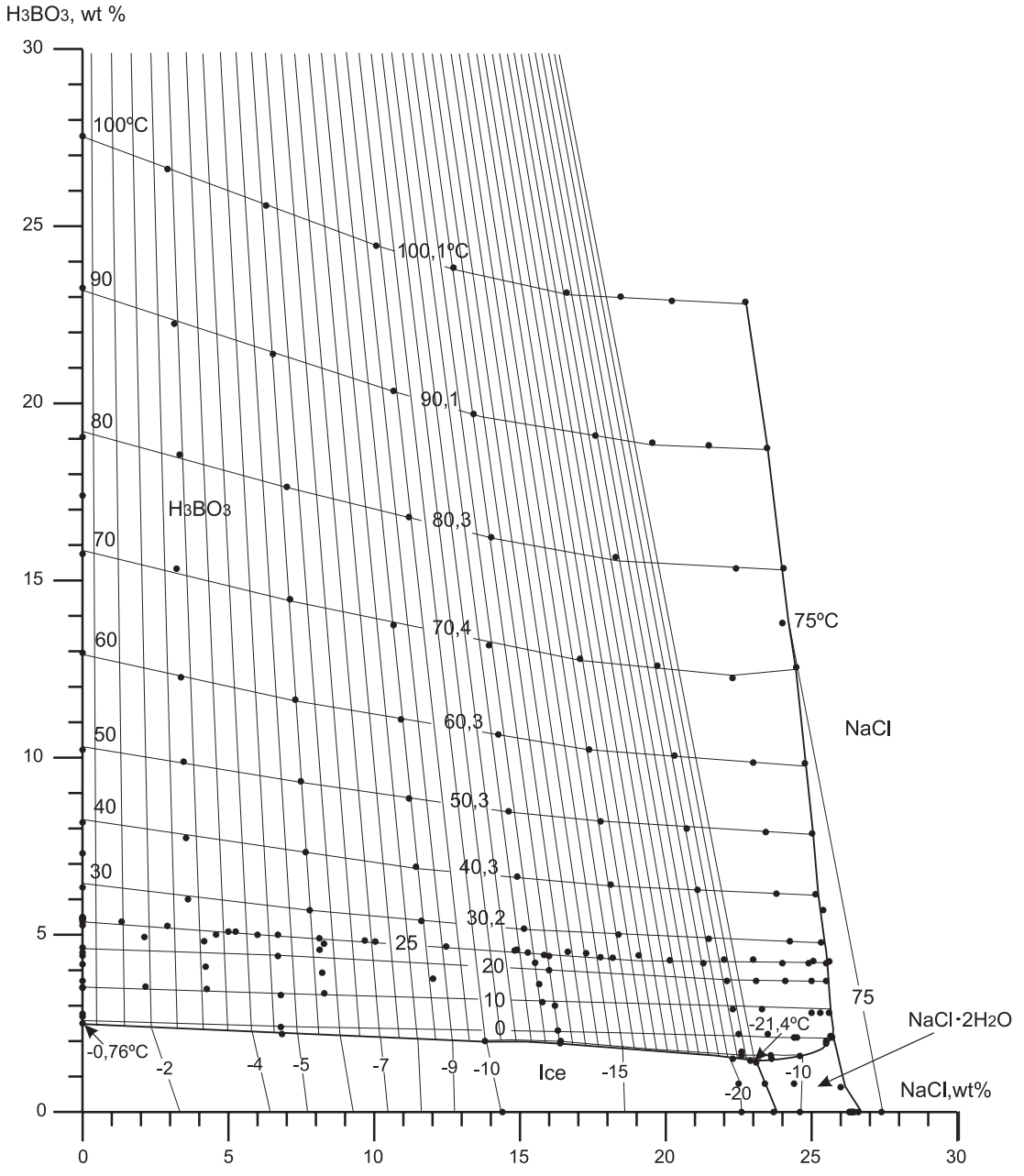

Fig. 4. Solubility diagram for the system $NaCl–H_3BO_3–H_2O$ in the coordinates $NaCl–H_3BO_3$. Straight lines starting from ice–sassolite-solution equilibrium curve show compositional variations after ice melting for fluid inclusions with daughter sassolite (modified after Peretyazhko et al., 2000). These lines are constructed for different ice melting temperatures with 0.5 °C increment. The temperature dependences of NaCl and H_3BO_3 concentrations are approximated by equations calculated from experimental data. For ice–sassolite-solution equilibrium: NaCl, wt.% = $-1.495-2.058\times T-61.284\times 10^{-3}\times T^2-8.73\times 10^{-4}\times T^3$; H_3BO_3, wt.% = $2.504+82.132\times 10^{-3}\times T+47.532\times 10^{-4}\times T^2+1.531\times 10^{-4}\times T^3$. For sassolite–halite-solution equilibrium: NaCl, wt.% = $25.694-7.605\times 10^{-3}\times T-51.174\times 10^{-6}\times T^2-1.491\times 10^{-6}\times T^3$; H_3BO_3, wt.% = $2.093+64.796\times 10^{-3}\times T+63.977\times 10^{-5}\times T^2+7.487\times 10^{-6}\times T^3$, where T stands for temperature in degrees of Celsius.

studied quartz from pegmatite intergrowths and base parts of the pocket crystals and have not found inclusions aligned along the growth zones. The inclusions arranged along the linear zones intersecting the grain boundaries were regarded as secondary or pseudo-secondary. These criteria accord well with the general principles advanced by Ermakov (1972) and Roedder (1984). The FI and MI confined to the same cluster (Fig. 5c) of inclusions were interpreted as co-genetic, i.e. as simultaneously trapped inclusions of coexisting melts and fluids.

The quartz grains from the quartz–oligoclase host pegmatite contain small (1–5 μm) primary MI, which consist of a solid phases not identifiable by the applied methods. The fluid isolations containing liquid and gas bubbles can be readily observed in larger (about 5 μm) inclusions. The term "fluid isolation" hereinafter means a part of melt inclusion consisting of an aqueous liquid, a gas and sometimes a daughter crystal, which dissolves in aqueous phase on heating. Several quartz plates contained primary FI, which were identified only due to the flickering of a gas bubble in the inclusion. Secondary fluid inclusions are sparse.

The quartz grains from the quartz–albite pocket wall assemblage contain clusters of 100 μm and larger MI (Fig. 5a). They consist of a silicate crystalline phase and fluid isolation (gas + liquid + daughter crystal). Those inclusions are not associated with smaller ones (up to 10 μm). The euhedral druse quartz contains large MI and abundant primary, secondary and pseudo-secondary FI (Fig. 5b–d). Significant variations of fluid/silicate volume ratios are typical of coeval MI (Fig. 5b, c, e–j). These observations, in our opinion, confirm the heterogeneous or mixed nature of large MI in miarolitic quartz. In other words, such inclusions resulted from simultaneous entrapment of coexisting melts and fluids. Hereafter, we will refer to those inclusions as fluid-melt inclusions (FMI) to stress their mixed nature.

FMI in the bottom parts of pocket quartz crystals and in the quartz from the quartz–albite assemblage are dominated by silicate crystalline phases (Fig. 5a). The fluid isolations of the FMI in that zone are usually invisible. The volume fraction of fluid in a FMI increases noticeably toward the intermediate growth zone of the pocket quartz. The fluid isolation contains an aqueous phase, crystals of sassolite (H_3BO_3) and a gas bubble (Fig. 5b–d). The amount of FMI rapidly decreases, compared to FI, in the same way and they do not occur in the latest growth zone of the pocket quartz. Several FI contain both sassolite and unknown daughter crystals (Fig. 5j), which may result from crystallization of small melt droplets or heterogeneous entrapment of coeval solid phases.

5.2. Phase composition at room temperature

Raman spectroscopy identified mica minerals, probably muscovite and lepidolite, in the crystal aggregates in FMI from the pocket quartz (muscovite has an intense band at 400 cm^{-1} and a weak band about 702 cm^{-1}, while lepidolite has an intense band at 712 cm^{-1} and a very weak band at 400 cm^{-1}). In several opened MI, the compositions of daughter micas were determined by EMPA. Micas in the same MI have strongly variable F and Cs contents (Tables 1a and 1b). The concentration of Cs_2O increases up to 20–24 wt.% towards the outermost zones of the mica plates. The analytical totals are less 100% probably due to elevated H_2O, Li and B contents in the micas. SIMS data showed that mica in one opened inclusion contain 3.1 wt.% H_2O, 1.9 wt.% B_2O_3, and 3.2 wt.% Li_2O. Therefore, we suggest that the mica assemblage in FMI consists of lepidolite and a mica mineral of an intermediate composition between muscovite, boromuscovite $KAl_2[BSi_3O_{10}](OH,F)_2$, nanpingite $CsAl_2[AlSi_3O_{10}](OH,F)_2$, and hypothetic boron nanpingite $CsAl_2[BSi_3O_{10}](OH,F)_2$. EMPA and SEM EDS data show that crystalline phases in many FMI contain topaz, potassium feldspar, probably tourmaline (optically identifiable) and several unidentified minerals. Besides the daughter minerals, FMI may contain daughter quartz deposited onto the inclusion walls (Fig. 6).

Topaz and tourmaline occur as crystalline inclusions in quartz. Topaz is scarce in the latest zones of the quartz–oligoclase pegmatite and more abundant in the quartz–albite assemblage of the pocket walls. In the pocket wall quartz, topaz is usually associated with FMI and MI. The volume fraction of topaz is variable; in many places topaz crystals protrude outside from inclusions, deep into the host mineral. The microscopic observations and microthermometry data, to be reported below, allow the suggestion that topaz was entrapped as a crystalline phase coexisting with melt and fluid.

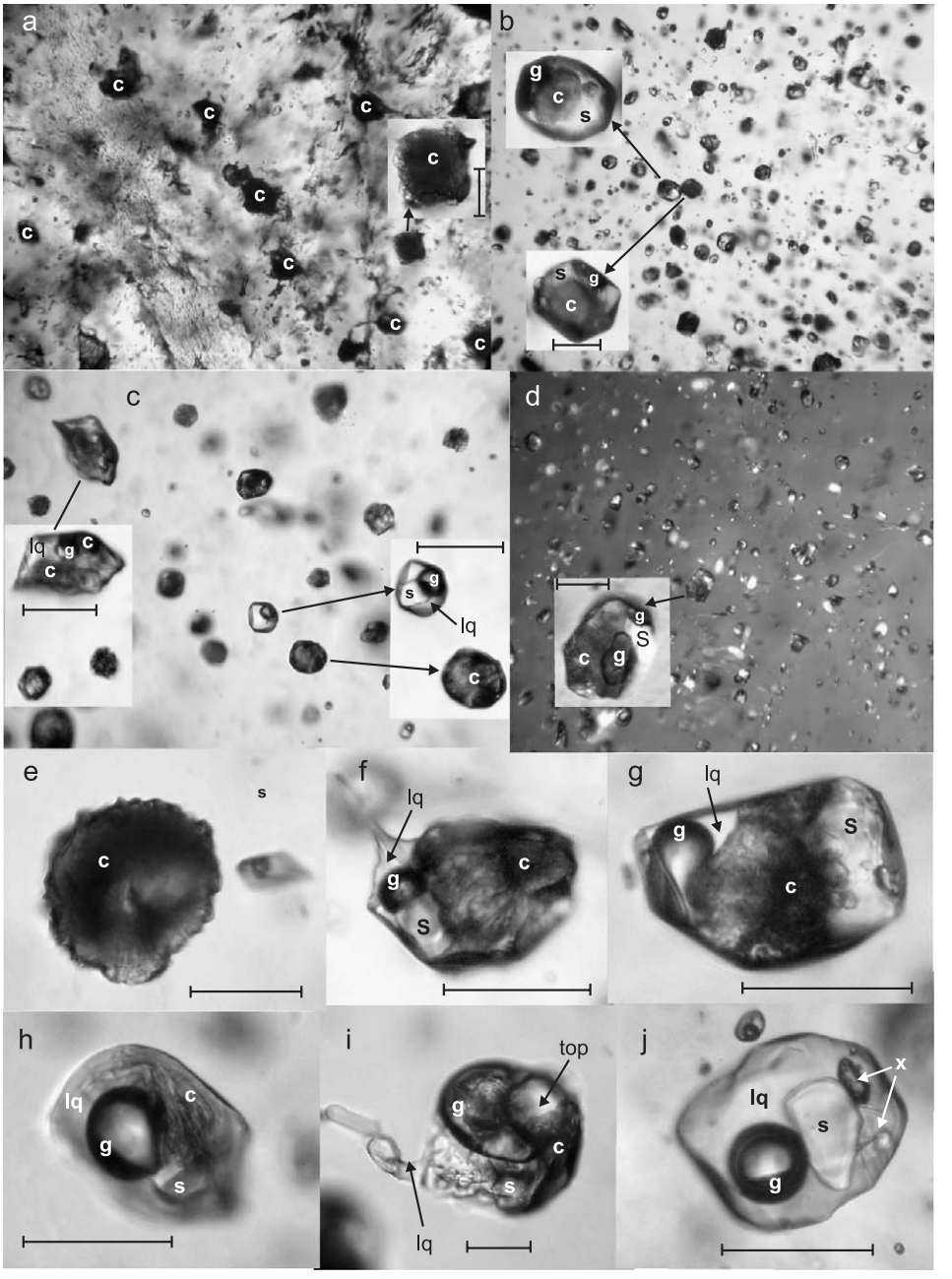

Fig. 5. Fluid-melt (FMI) and fluid (FI) inclusions: a—FMI in quartz from quartz–albite assemblage of the pocket wall are filled with crystalline aggregate; b,c—co-genetic FMI and primary FI in the base of pocket quartz crystal; d—rare FMI among numerous FI in the middle part of pocket druse quartz (crossed polars, the bright spots-daughter sassolite crystals); e–i—FMI in pocket quartz with different volume fractions of silicate crystalline phases, aqueous phase, gas bubble, sassolite and topaz; j—FI with daughter sassolite and some undetermined minerals (×) in pocket druse quartz. c—silicate crystal aggregate, g—gas bubble, lq—aqueous solution, s—sassolite, top—topaz. Scale bar is 50 μm.

Table 1a
Average compositions of accessory tantaloniobates and cassiterite from pocket and pocket-hosting assemblages (wt.%)

	1(4)	2(6)	3(4)	4(1)	5(5)	6(1)
WO_3	28.54	27.11	29.47	6.42	2.11	0.02
Ta_2O_5	7.78	10.73	12.32	19.42	6.26	1.98
Nb_2O_5	31.60	33.15	32.38	53.56	67.36	0.14
TiO_2	2.24	1.67	1.11	2.24	0.74	0.62
SnO_2	0.38	0.41	0.45	0.26	0.03	96.74
Sc_2O_3	0.41	0.37	0.17	n.d.	0.40	n.d.
CaO	0.02	0.02	n.d.	n.d.	0.29	n.d.
FeO	8.28	2.68	2.74	5.15	2.33	0.00
MnO	11.41	17.03	18.15	13.71	16.54	0.11
Σ	90.66	93.17	96.79	100.76	96.06	99.61

1–9—accessory minerals: 1–3—W-rich tantaloniobate, 4,5—W-rich tantalite–columbite, 6—cassiterite, 7—garnet, 8—topaz, 9—lepidolite; 10–14—daughter phases of fluid-melt inclusions: 10—topaz, 11–14—micas of muscovite–nanpingite series (boron-rich), In brackets—number of electron microprobe analyses, analyst Pospelova L.N. (UIGGM RAS, Novosibirsk). n.d.—not determined.

Since the line at 880 cm^{-1} is usually present in the Raman-spectra of the FMI that are free of visible aqueous phases, the aqueous solution of H_3BO_3 and the daughter sassolite must occur in interstices of silicate solid phases. The FI (Fig. 5c) associated with FMI contain boric acid solutions, gas bubbles and daughter sassolite. Raman spectroscopy revealed no significant amounts of CO_2, CH_4, H_2S and N_2 in the gaseous phase of FI.

5.3. Microthermometry

The melting of small (1–2 μm) MI in the host pegmatite quartz starts at 500–550 °C. The last phase—a fluid bubble—disappears at 570–600 °C. The quenched MI had remained homogeneous for several months at room temperature. Most larger inclusions (2–5 μm) showed decrepitation at heating. There are few, if any, micron-sized inclusions in druse quartz which are hidden by larger fluid inclusions making the former inaccessible for microthermometry.

Comparatively large FMI (20–100 μm) in druse quartz showed the first signs of melting after quenching at 550–580 °C at an external pressure of 2.5 kbar. The last silicate phase disappeared at 615 °C in several relatively small (20–50 μm) FMI and in those containing large fluid isolations. The majority of other FMI contain variable amounts of unmelted daughter crystals. The remaining crystals in those inclusions had not been completely melted even after overheating at 650 °C and 2.5 kbar for 24 h. This can be explained by insufficient durations of autoclave runs for large FMI.

After the final quenching, we observed inclusions containing glass + unmelted crystals ± fluid (gas) (Fig. 7a,b) and glass + fluid isolations (liquid + gas + sassolite) (Fig. 7c). Mica minerals and topaz were identified as unmelted crystals. Topaz shows no traces of dissolution.

Table 2 shows the microthermometry data on FI and fluid isolations in FMI, H_3BO_3 contents and total salinities (wt.% of NaCl-eq.). The evidence for low total salinities of the fluids entrapped by FI and FMI comes from relatively high ice melting temperatures. Several inclusions without traces of decrepitation during autoclave runs were selected for microthermometric studies. After heating in the autoclave, the temperature of homogenization of fluid isolations in FMI increased from 250–300 to 350 °C. This suggests a decrease of the fluid density probably due to partial dissolution of water in the melt. Fluids of FMI and associated FI have similar compositions (Table 2). Microthermometry of fluid phases of FMI revealed that the ice-melting and sassolite-dissolution

Table 1b
Average compositions of accessory silicates from pocket and pocket-hosting assemblages and daughter silicate phases of the fluid-melt inclusions (wt.%)

	7(3)	8(2)	9(16)	10(5)	11(8)	12(2)	13(4)	14(7)
SiO_2	36.28	31.04	57.11	32.89	45.67	39.63	40.90	43.08
Al_2O_3	20.42	53.89	18.69	56.30	31.40	26.05	19.66	16.02
CaO	0.48	0.01	0.01	0.00	0.01	0.06	0.12	0.02
FeO	22.52	0.01	0.09	0.00	0.00	0.00	0.00	0.00
MnO	19.82	0.00	0.07	n.d.	0.00	0.01	0.04	0.04
Na_2O	0.12	0.01	0.14	0.01	0.45	0.99	0.77	0.22
K_2O	0.00	0.01	11.00	0.00	10.33	5.95	3.56	1.76
Rb_2O	0.00	0.02	0.37	0.00	0.21	0.23	0.23	0.26
Cs_2O	0.00	n.d.	0.89	0.01	0.18	5.71	15.06	22.66
F	n.d.	17.81	11.17	18.11	1.78	2.40	5.11	6.70
Σ (−O = F_2)	99.64	95.30	94.84	99.69	89.28	80.01	83.18	87.94

1–9—accessory minerals: 1–3—W-rich tantaloniobate, 4,5—W-rich tantalite–columbite, 6—cassiterite, 7—garnet, 8—topaz, 9—lepidolite; 10–14—daughter phases of fluid-melt inclusions: 10—topaz, 11–14—micas of muscovite–nanpingite series (boron-rich), In brackets—number of electron microprobe analyses, analyst Pospelova L.N. (UIGGM RAS, Novosibirsk). n.d.—not determined.

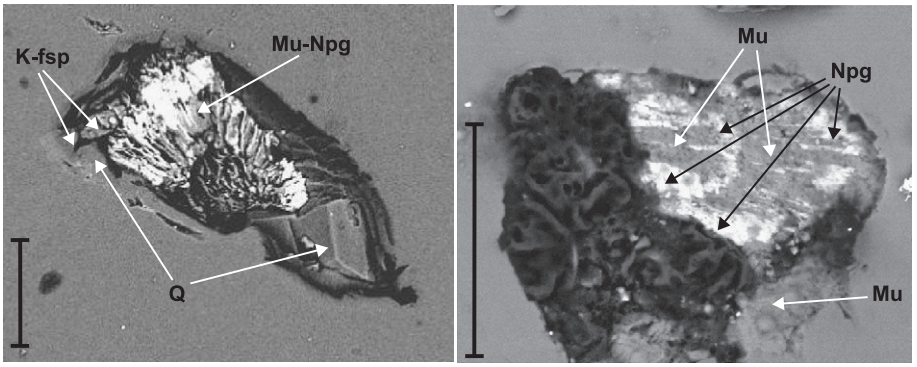

Fig. 6. Backscattered electron images of opened unheated fluid–melt inclusions. Daughter phases: Q—quartz, K-fsp—potassium feldspar, Mu—aggregate of muscovite and Cs-rich muscovite, Npg—nanpingate in outer zones of muscovite crystals. Scale bar is 50 μm.

temperatures do not change significantly after heating in the autoclave. This may be explained by a heterogeneous nature of the studied FMI and proportional dissolution of NaCl and orthoboric acid components in the melt.

5.4. Composition of re-melted glasses

Three 40-μm FMI that are almost free of unmelted daughter crystals (< 10 vol.%) were selected for compositional studies of late pegmatitic melts. EMPA and SIMS analyses (Table 3) show that the glasses in the FMI are low-silica, slightly peraluminous, and contain increased contents of F, B, H_2O and extraordinarily high Cs contents. The concentrations of femic components are negligible. The studied glasses are special for their negligible Cl and P contents—below the detection limit of EMPA. Low Na_2O (Table 3, an.1–3) is probably due to a loss of alkali metals (especially Na and K) in the course of EMPA analysis of water-bearing aluminosilicate glasses. To avoid the loss of alkalis, Morgan and London (1996) recommended use of a defocused electron beam and a low beam currents. In this study we applied a 20 μm electron beam and 10 nA beam current. Chupin and Titov (Chupin, pers. comm.) detected 10 rel.% of Na_2O loss analyzing hydrous aluminosilicate glass (H_2O—6 wt.%, Na_2O—4.3 wt.%) by electron beam defocused to 20 μm at 40 nA current. This is in good agreement with estimations that Morgan and London (1996) made for 7 wt.% H_2O glass. They reported 8.3 rel.% underestimation of Na_2O at 10 nA beam current and 12 rel.% at 20 nA beam current. Thus, we expect that Na migration during EMPA analysis under applied con-

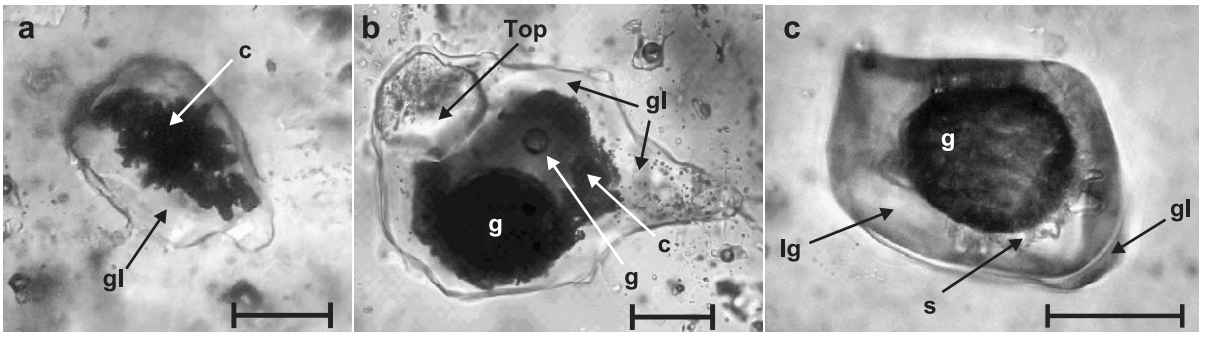

Fig. 7. Fluid-melt inclusions in the basal zones of the druse quartz after re-melting in autoclave. Quench temperature is 640 °C and pressure is 2.5 kbar. a—FMI consist of glass and un-melted muscovite crystals, b—FMI consist of glass with gas bubbles, and un-melted muscovite and topaz; c—FMI consist of large fluid isolation (aqueous solution, gas bubble, and sassolite) and thin rim of homogeneous silicate glass. c—crystal aggregate, g—gas bubble, lq—aqueous solution, s—sassolite, top—topaz, gl—glass. Scale bar is 50 μm.

Table 2
Microthermometry of fluid inclusions and fluid isolations in melt inclusions

	$T_{eut.}$, °C	T_{ice}, °C	$T_{sas.}$, °C	$T_{hom.}$,°C	$C_{H_3BO_3}$, wt. %	C_{NaCl} eq., wt.%
Fluid inclusions	−6.5 ÷ −28	−2.9 ÷ −6.5	59 ÷ 88	220 ÷ 360	12–20	4.6 ÷ 9.4
Fluid in melt inclusions	−9.5	−3.7 ÷ −7.6	70 ÷ 80	250 ÷ 300	15–17	5.7 ÷ 9
		−4.2[a]	72[a]	350 ÷ 355[a]	15.4[a]	5.4[a]

[a] After quench in autoclave at 650 °C and 2.5 kbar. The H_3BO_3 and salt concentrations were estimated by method described by Peretyazhko et al. (2000) and Smirnov et al. (2000).

ditions could result in about 10 rel.% underestimation of Na_2O content. Glass 3 (Table 3) was studied one more time under the same EMPA conditions as well as by SIMS method (analysis 4, Table 3). The SIMS study showed that this glass also contains Li, Be, Ta and Nb. However, even considering the water content of 5.67 wt.% measured by SIMS, the totals of the analysis are significantly less than 100%. This deficiency is probably due to the loss of water during the SIMS analysis of the glass. Ihinger et al. (1994) reported that the accuracy of water measurement decreases at a content of H_2O in glasses exceeding 5 wt.% due to a high amount of molecular H_2O, which cannot be measured by SIMS. Thus, the anticipated content of H_2O in the glasses of inclusions containing unmelted crystalline phases could exceed 12 wt.%. An addition of 10 wt.% of unmelted micas will not significantly decrease this estimation of the H_2O content, however, it may appear a little lower due to the dissolution of quartz from the inclusion walls. Boron in compositionally similar glasses probably occurs as $B(OH)_3$ (Veksler et al., 2002). Some boron might have been lost with evaporated H_2O in the process of SIMS analysis due to the high volatility of orthoboric acid with water vapor and therefore the content of B_2O_3 in the glass (Table 3, an.4) may be also underestimated.

6. Calculation of isochores and density of aqueous boric acid fluids

One of the most important and difficult problems of this study is estimation of the pressure change during pocket formation. Pressure is traditionally estimated based on the microthermometric data on fluid inclusions and PTVX properties of fluids of a known composition. The majority of geological processes with participation of aqueous fluids are well approximated by the chloride–salt–H_2O or chloride–salt–H_2O–CO_2 systems, whose properties are well defined experimentally or empirically. Our results indicate that FI and FMI in miarolitic quartz contain fluids whose major solute is boric acid rather than chloride salts. Therefore, the effect of H_3BO_3 on the PTV properties of aqueous solutions must be assessed prior to the estimation of pressure.

Table 3
Composition of quenched melt inclusion glasses (wt.%)

	1	2	3	4	5	6
SiO_2	58.26	58.81	57.55	58.21	56.9	60.07
Al_2O_3	12.59	13.06	12.64	12.62	11.4	17.85
CaO	0.08	0.03	0.16	0.16	0.03	0.04
FeO	b.d.l.	b.d.l.			0.24	0.17
MnO	b.d.l.	b.d.l.			0.04	0.02
BeO				**0.12**	0.30	
Na_2O	0.51	0.27	0.61	1.41	2.04	4.97
K_2O	2.58	1.77	3.29	4.10	4.33	4.00
Rb_2O	0.10	0.10	0.05	**0.14**	1.10	
Cs_2O	4.46	3.64	4.77	5.20	1.59	
Li_2O				**0.54**	0.57	
B_2O_3				**2.51**	3.70	
Ta_2O_5				**0.57**		
Nb_2O_5				**0.10**		
P_2O_5				b.d.l.	1.14	0.00
F	1.94	2.36	2.63	2.73	2.45	5.11
Cl	b.d.l.	b.d.l.		n.d.	0.10	0.33
H_2O				**5.67**	16.2	6.48
Σ (−O=F_2)	79.7	79.05	80.59	92.93	100.98	96.89

1–4—glasses of MI, quenched at 650 °C and 2.5 kbar. Phase composition of inclusions: 1,2—glass + not completely melted crystals; 3,4—glass + not completely melted crystals + gas bubble; 5—glass of melt A inclusions in quartz from pegmatites of Ehrenfriedersdorf Sn–W deposit, Germany (Thomas et al., 2003); 6—glass of melt inclusion in topaz from topaz–beryl miarolitic pegmatite, Volyn, Russia (Kovalenko et al., 1996). SIMS data are marked in bold (analyst S.A. Simakin, IM RAS, Yaroslavl), the rest-electron microprobe analyses (analyst Pospelova L.N., UIGGM RAS, Novosibirsk). b.d.l.—below detection limit. Low Na_2O in analyses 1–3 is probably due to a loss of Na in the course of EMPA analysis. Underestimation of Na_2O in an. 4 is not greater than 10 rel.% due to application of defocused electron beam and low beam current. See details in the text.

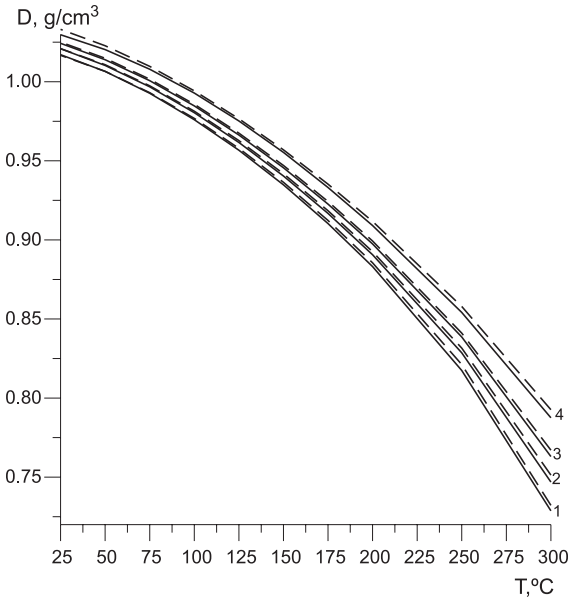

Fig. 8. Comparison of experimentally determined densities of 0.7 m H_3BO_3 aqueous solution within 25–300 °C (Azizov and Akhundov, 1996) (solid lines) with densities, calculated using SELECTOR software (dashed lines). Numbers indicate pressures in bars: 1–100; 2–200; 3–300; 4–500.

The few experimental data on the properties of boric acid solutions are restricted to a relatively low-temperature (25–300 °C) and low-pressure (100–500 bar) region (Azizov and Akhundov, 1996). The data on PVTX properties of boric acid salt-bearing systems are absent in the literature. Since NaCl-like salts do not form aqueous complexes with H_3BO_3, the volumetric properties of the resultant fluid shall depend on the volumetric properties of the H_2O–H_3BO_3 and NaCl–H_2O solutions in a proportional-additive manner.

The densities and PTV properties of boric acid aqueous fluids were calculated for a temperature range of 100 to 700 °C and up to 10 kbar pressures (Peretyazhko and Zagorsky, 2002) with a help of SELECTOR software created by Karpov et al. (1997). Thermodynamic parameters of sassolite, H_2O, H_2, O_2, OH^-, H^+, $B(OH)_3^\circ$ and $B(OH)_4^-$ aqueous complexes, BO_2^-, and 23 B-bearing ideal gases were acquired from NIST-JANAF Thermochemical Tables (1998) and Pokrovski et al. (1995) and were used as a database for numerical modeling. Gibbs isobaric–isothermal potential minimization $G(T,P)$ of the H_2O–H_3BO_3 system within a given T–P range revealed that $B(OH)_3^\circ$ is a major aqueous complex (pH = 3.4–4.4) and a main gas component along with H_2O vapor. Besides, the vapor phase contains $H_3B_3O_6$ and BO_2^- but their contributions to the total vapor pressure do not exceed a few percent. The calculation of volumes, densities and pressures of the fluids has not considered B-bearing ideal gases because their critical parameters are unknown. The modeled solubility of H_3BO_3 in saturated aqueous solutions is consistent with the reference data cited in Zhdanovskii et al. (1975) with 4.64–35.19 wt.% H_3BO_3 solutions at 20–120 °C. The calculated densities accord well with the experimental results obtained by Azizov and Akhundov (1996) for 0.7 m H_3BO_3 (4.2 wt.%) solution at a temperature range of 25–300 °C and a pressure range of 100–500 bar (Fig. 8). Thus, we suggest that the densities and pressures of boric acid

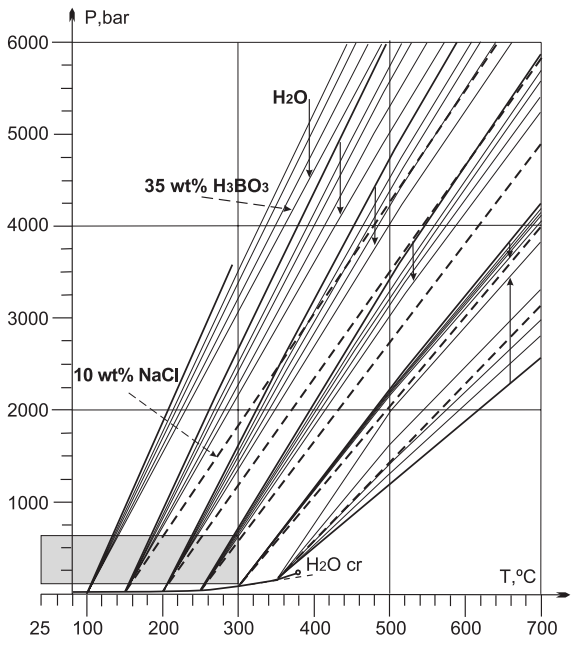

Fig. 9. Calculated vapor–liquid curves and isochores of the H_2O–H_3BO_3 system for H_3BO_3 content 0, 12.96, 19.05, 27.54, and 35.19 wt.% (after Peretyazhko and Zagorsky, 2002). Here and in Figs. 10 and 12 the arrows show increase of H_3BO_3 concentration in the fluids. Isochores of 10 wt.% NaCl aqueous solution by Naumov (1982) are shown for comparison by dashed lines. H_2O cr—critical point of pure water. The box outlines the area used for verification of the model by experimental data shown in Fig. 8.

aqueous fluids calculated for elevated temperatures and pressures are reliable.

The $P-T$ gas–liquid equilibrium parameters of boric acid saturated aqueous solutions, ranging from 4.6 to 35.2 wt.% H_3BO_3, and the densities of the liquids were calculated based on $G(T,P)$ potential minimization (Fig. 9, Table 4). Using an isochoric Helmholtz potential $A(T,V)$ minimization and equilibrium vapor–liquid volumes obtained from the $G(T,P)$ minimization, the fluid pressures and the angles of isochores (dP/dT) were calculated for temperatures up to 700 °C (Table 5). At higher temperatures and pressures, the isochores become nonlinear (Fig. 9). The isochores for pure water and 10 wt.% NaCl aqueous solutions are shown for comparison. The angles of the isochores (dP/dT) for $H_3BO_3-H_2O$ fluids obviously differ from those of the NaCl–H_2O system for homogenization temperatures ($T_{hom.}$) of 100–300 °C. This makes the fluid pressure estimations for boric acid solutions based on the NaCl–H_2O system incorrect. The $H_3BO_3-H_2O$ isochores plot closer to the H_2O isochores, however, the angles of the latter are steeper than those of the former. In the high-temperature region, the difference between dP/dT of H_2O and $H_3BO_3-H_2O$ isochores gets less pronounced, but it remains notable between $H_3BO_3-H_2O$ and NaCl–H_2O isochores. The isochores of boric acid solutions and H_2O are very similar at $T_{hom.} \approx 300$ °C. At $T_{hom.} = 305$ °C, the dP/dT value remains constant and does not depend on the H_3BO_3 content in the fluid and its temperature (Fig. 10). For solutions with higher homogenization temperatures, the $H_3BO_3-H_2O$ isochores get steeper than the H_2O isochores that is typical of many salt-water systems (Samoilovich, 1969; Naumov, 1982) as illustrated by a correspondent isochore of the NaCl–H_2O system (Fig. 9).

As far as aqueous alkali-chlorides and orthoboric acid may have an effect on the fluid pressure, we may conclude that addition of H_3BO_3 into an aqueous system with homogenization temperatures of 100 to 300 °C increases the pressure compared to aqueous NaCl systems. The $H_3BO_3-H_2O$ fluids that homogenize into liquid at $T_{hom.}$>305 °C produce pressures

Table 4
Density of liquid and pressure of boric acid solutions at liquid–vapor boundary

T, °C	H_3BO_3 concentrations, wt.% (temperature of sassolite dissolution, °C)						
	H_2O	4.64 (20)	8.17 (40)	12.96 (60)	19.05 (80)	27.54 (100)	35.19 (120)
	Fluid density, g/cm^3; Pressure, bar						
100	0.958	0.974	0.986	1.003	1.025	1.058	1.091
	1.0	1.0	1.0	1.0	1.0	1.0	1.0
125	0.939	0.955	0.967	0.984	1.006	1.039	1.071
	2.3	2.3	2.3	2.3	2.3	2.3	2.3
150	0.917	0.933	0.945	0.962	0.985	1.018	1.051
	4.8	4.8	4.8	4.8	4.8	4.8	4.8
175	0.892	0.908	0.921	0.938	0.961	0.996	1.029
	8.9	8.9	8.9	8.9	8.9	8.9	8.9
200	0.865	0.881	0.894	0.912	0.936	0.971	1.005
	15.6	15.6	15.6	15.6	15.6	15.6	15.6
225	0.834	0.849	0.863	0.882	0.906	0.943	0.979
	25.5	25.0	24.7	24.2	23.5	22.3	21.1
250	0.799	0.816	0.830	0.849	0.875	0.913	0.951
	39.8	39.1	39.3	38.2	37.9	36.9	33.4
275	0.759	0.777	0.789	0.810	0.837	0.878	0.917
	59.5	58.3	57.3	55.9	54.1	51.1	47.8
300	0.712	0.731	0.746	0.767	0.796	0.840	0.884
	85.9	84.1	83.8	82.7	78.6	74.2	69.4
325	0.655	0.675	0.691	0.715	0.747	0.798	0.850
	121	118	115	112	107	100	93
350	0.575	0.601	0.623	0.656	0.703	0.780	0.867
	165	161	157	151	143	131	121

Table 5
Angles (dP/dT) of liquid isochores (bar/°C) in different temperature ranges

$T_{hom.}$, °C	H_3BO_3 concentrations, wt.% (temperature of sassolite dissolution, °C)						
	H_2O	4.64 (20)	8.17 (40)	12.96 (60)	19.05 (80)	27.54 (100)	35.19 (120)
100–300 °C							
100	18.680	18.295	17.990	17.550	16.955	16.040	15.400
125	18.330	17.947	17.632	17.187	16.587	15.655	14.724
150	17.762	17.388	17.088	16.662	16.082	15.188	14.288
175	16.993	16.657	16.385	15.993	15.465	14.641	13.809
200	16.045	15.755	15.525	15.185	14.725	14.005	13.265
225	14.900	14.480	14.377	14.224	13.793	13.196	12.705
250	13.564	13.398	13.294	13.116	12.862	12.462	12.072
275	11.990	11.828	11.468	11.724	11.596	11.556	11.288
300	10.665	10.635	10.626	10.605	10.572	10.514	10.488
300–500 °C							
100	18.065	17.800	17.585	17.270	16.825	16.120	15.430
125	17.061	17.340	17.130	16.820	16.380	15.690	14.960
150	17.045	16.790	16.580	16.280	15.855	15.190	14.495
175	16.370	16.125	15.930	15.650	15.250	14.625	13.965
200	15.570	15.350	15.170	14.910	14.550	13.980	13.385
225	14.630	14.400	14.270	14.055	13.735	13.230	12.730
250	13.515	13.370	13.245	13.070	12.825	12.425	12.005
275	12.215	12.105	11.985	11.900	11.735	11.485	11.185
300	10.665	10.635	10.626	10.605	10.572	10.514	10.448
325	8.917	8.989	9.034	9.154	9.291	9.560	9.866
350	6.824	7.093	7.349	7.758	8.465	9.958	12.405
500–700 °C							
100	15.530	15.375	15.245	15.055	14.785	14.340	13.895
125	15.220	15.060	14.925	14.730	14.455	14.000	13.515
150	14.830	14.665	14.535	14.340	14.065	13.615	13.120
175	14.355	14.200	14.065	13.870	13.600	13.160	12.690
200	13.785	13.630	13.500	13.320	13.065	12.645	12.200
225	13.095	12.930	12.825	12.670	12.425	12.040	11.645
250	12.275	12.155	12.055	11.915	11.710	11.380	11.025
275	11.300	11.200	11.095	11.010	10.850	10.600	10.315
300	10.140	10.085	10.050	9.985	9.895	9.750	9.580
325	8.730	8.745	8.750	8.775	8.795	8.840	8.870
350	6.920	7.095	7.245	7.480	7.830	8.455	9.230

The fluid pressure under isochoric conditions in liquid field can be calculated combining data of Tables 4:

$T = 100–300$ °C: $P = P_{l\text{-}v} + (T - T_{hom.})dP/dT_{100-300\ °C}$.

$T = 300–500$ °C, $T_{hom.} < 300$ °C: $P = P_{l\text{-}v} + (300 - T_{hom.})dP/dT_{100-300\ °C} + (T - 300)dP/dT_{300-500\ °C}$.

$T = 300–500$ °C, $T_{hom.} > 300$ °C: $P = P_{l\text{-}v} + (T - T_{hom.})dP/dT_{300-500\ °C}$.

$T = 500–700$ °C, $T_{hom.} < 300$ °C: $P = P_{l\text{-}v} + (300 - T_{hom.})dP/dT_{100-300\ °C} + 200dP/dT_{300-500\ °C} + (T - 500)dP/dT_{500-700\ °C}$.

$T = 500–700$ °C, $T_{hom} > 300$ °C: $P = P_{l\text{-}v} + (500 - T_{hom.})dP/dT_{300-500\ °C} + (T - 500)dP/dT_{500-700\ °C}$.

T—temperature for which the pressure is to be calculated, $T_{hom.}$—homogenization temperature, $P_{l\text{-}v}$—pressure at homogenization temperature.

higher than does the pure H_2O. Moreover, the density of orthoboric-acid aqueous fluids increases with concentration to a lesser extent than do the densities of NaCl, $CaCl_2$, KCl, LiCl, NH_4Cl, NaOH, Na_2CO_3, and K_2CO_3 solutions. Therefore, the positions of H_3BO_3–H_2O and salt–H_2O isochores will be notably different, especially at high P and T.

The obtained microthermometric data (Table 2) show that orthoboric acid is a dominating solute of the fluid participating in the formation of miarolitic cavities (up to 20 wt.%), whereas the content of other components is less than 9 wt.%. Thus, we believe that it is more correct to estimate the fluid pressure with the H_3BO_3–H_2O system. The estimated pressures may appear overestimated because at this point we cannot determine the effect of other salts on the system. On the other hand, as far as the salts are present in low concentrations, we suggest no significant differences between the modeled and actual pressures.

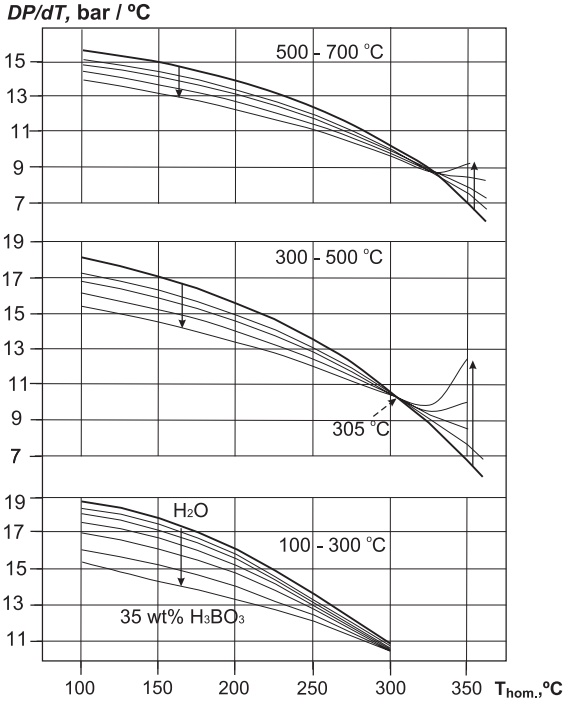

Fig. 10. Isochore angles (dP/dT) as a function of homogenization temperature ($T_{hom.}$) (modified after Peretyazhko and Zagorsky, 2002).

7. Discussion

The previous works have reported that the formation of miarolitic cavities starts at the latest stage of crystallization of pegmatitic magma (Kosukhin et al., 1984; Bakumenko and Konovalenko, 1988; Kovalenko et al., 1996). The available data on the conditions of pocket formation are scarce and limited for the its latest hydrothermal stage (Zagorsky et al., 1999b). Kosukhin et al. (1984) and Kovalenko et al. (1996) suggest that the late melts of intra-granitic rock crystal (± fluorite) and topaz–beryl miarolitic pegmatites are the most evolved derivatives of a parent volatile-rich granitic magma. The recent experimental studies performed by Veksler et al. (2002) suggest that, under certain PTX conditions, F-, B-, and P-rich aluminosilicate melts, so-called hydrosaline melts, and aqueous boric acid fluid can coexist near the solidus of the pegmatitic melt. Thus, the formation of miarolitic cavities includes a great variety of physical–chemical processes and mineral-forming media. The tentative model below illustrates PTX conditions, aggregate states[2] and other agents of pocket formation.

7.1. Aggregate state and chemical composition of the mineral-forming media

Co-genetic FI and MI in quartz of the pocket and host oligoclase pegmatite, and complex fluid-melt inclusions in the basal parts of the pocket quartz suggest that at least two immiscible liquids—aluminosilicate melt and boric acid aqueous fluid—took part in pocket formation at its early stages. The compositions of quenched FMI glasses (Table 3) and the domination of Cs-, F-, B-rich micas in the daughter mineral assemblage indicate unusual compositions of primary aluminosilicate melts, which were possibly strongly enriched in H_2O, B, F and granitophile rare elements (e.g. Cs, Li, Be, Ta, Nb). Those latest melts contain one or two orders of higher concentrations of rare elements than the bulk Malkhan pegmatite (Zagorsky and Peretyazhko, 1992a,b).

The compositions of quenched FMI glasses are generally similar to those of MI glasses (Table 3, an.5) in quartz from a pegmatite of the Ehrenfriedersdorf tin–tungsten deposit, Saxony area, Germany (Thomas et al., 2000). Our studied glasses compositionally differ from Ehrenfriedersdorf glasses: they have higher Cs and Li contents and no Cl, P and Sn. The MI glasses of Volyn topazes, Ukraine (Kovalenko et al., 1996), which also originated from late pegmatitic melts, contain more Cl and F, but are depleted in B and alkalis (Table 3, an.6). The studied latest melts have less SiO_2 and much more H_2O, B, F and alkali than the bulk pegmatite or granite. Thomas et al. (2000, 2003) have reported an extreme H_2O enrichment of the latest pegmatitic melts. This may be explained by an increased H_2O solubility in granitic melts due to high B and F contents (Pichavant, 1987; Manning et al., 1984; Morgan, 1991; London, 1999). Thus, the B and F enrichment of sub-rare-metal topaz–beryl and tourmaline-rich pegmatites and fluorine enrichment of fluorite-bearing rock crystal pegmatites must have had a special effect on the process of miarolitic pocket formation.

The microthermometry of co-genetic FMI and FI (Table 2) showed that the latest melts coexisted with boric-acid aqueous fluids of a total salinity of 4–8 wt.% NaCl-eq. and 12–16 wt.% H_3BO_3. The gradual decrease of FMI fraction in inclusion assemblages and the decrease of the fraction of solid phases in FMI suggest a preferential crystallization of the druse minerals from an aqueous fluid phase. We think that this may explain the above-mentioned discrepancy between druse minerals and daughter silicate minerals in FMI.

Based on the composition of the MI and their major daughter minerals, the crystallization of the latest melts would result in mica-rich mineral paragenesis. On the other hand, the pocket walls and druse assemblages are dominated by quartz and albite. Therefore, the crystallization of the studied melts could have produced minor amounts of Cs-rich micas and topaz in the pocket-wall assemblages. The evidence for strong element fractionation between immiscible phases comes from a wide occurrence of W-, Sn- and P-minerals. In spite of negligible concentrations of these components in the glasses of FMI, the pocket wall and druse mineral assemblages contain W-rich tantaloniobate, cassiterite, apatite and other phosphates. This is indicative of the preferential concentration of W, P and Sn in an aqueous fluid phase rather than in a silicate melt.

[2] Term "aggregate state" denotes a state of substance, which can be liquid, gaseous, solid or a mixture of all or some these phases.

7.2. P–T parameters of pocket formation

The microthermometric data on MI and FMI show that crystallization of the studied residual melt proceeded within a temperature range of 615 to 500 °C. The microthermomteric estimates for FMI and the modeled PVTX properties of boric-acid aqueous fluids (Table 4, Fig. 9) allowed us to assess the fluid pressure of pocket formation. The procedure of pressure estimation for one typical FMI from base part of a pocket wall quartz crystal is described below. At room temperature, this inclusion contains a silicate crystalline aggregate and a fluid isolation. The fluid isolation consists of boric-acid aqueous liquid, gas and daughter sassolite and homogenizes into liquid at 256 °C. The melting of the crystalline aggregate starts at 550 °C and finishes at 615 °C. After the final quench, the inclusion contains a silicate glass and a fluid isolation that homogenizes at 350 °C. Fig. 11 shows the isochores calculated for the fluid isolation before the start of the melting of the silicate phases (curve a–b, Fig. 11) and after their complete melting (curve c–d, Fig. 11). The pressure in the MI containing simultaneously trapped boric acid fluid and water-rich melt can increase from 2250 to 3730 bar at a temperature decreasing from 615 to 550 °C, i.e. the value of $\Delta P = P_{max} - P_o$ is about 1500 bar. It is important to note that the starting pressure is close to the lithostatic pressure of the formation of shallow-seated miarolitic pegmatites (Ginzburg and Rodionov, 1960; Černý, 1992). Fig. 11 (curve c–b) illustrates that the release of volatiles, firstly H_2O and H_3BO_3, from the melt during crystallization is responsible for the increase of intra-vacuole fluid density and, therefore, for the increase of pressure. Our calculation did not take into account the possible release of extra fluid by the melt or glass during or immediately after the quenching of FMI. Thus, the density of homogeneous fluid isolations may appear greater than the original density of the FMI fluid coexisting with the melt at $T = 615$ °C. In that case, the $P–T$ parameters of the homogeneous fluid coexisting with the residual melt would match a much shallower isochore than the curve c–d in Fig. 11 and, therefore, actual ΔP would be greater than that calculated.

7.3. Preliminary model and factors complicating the process of pocket formation

By analogy with MI, the crystallization of residual boron- and water-rich melts should increase the fluid pressure in miarolitic cavities according to the following model. Residual melts enriched in H_2O, B, F, Li, Cs and some other rare elements were separated in different parts of a pegmatite-enclosing chamber during late magmatic stage crystallization of a quartz–feldspar pegmatite matrix. The EMPA and SIMS analyses of the studied FMI glasses show that the H_2O content of their related melts may have exceeded 12 wt.%. According to Veksler et al. (2002) and Thomas et al. (2003), B-, F- and P-rich late aluminosilicate pegmatite melts may contain up to 43.8 wt.%

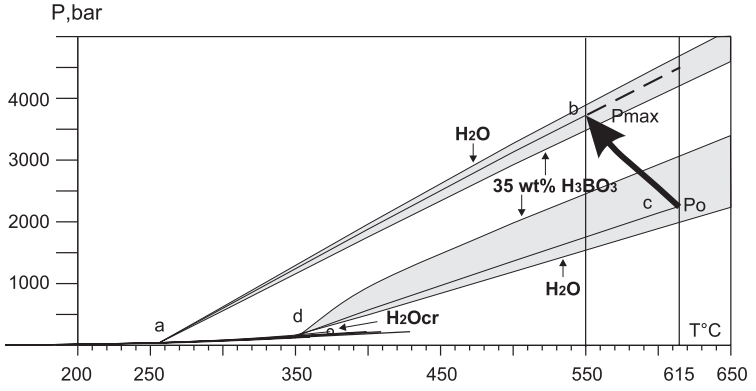

Fig. 11. Hypothetical $P–T$ path (black arrow) during crystallization of water saturated melt in FMI. Lines ab and cd are isochores of fluid isolation in B FMI before and after melting, respectively. The shaded areas show for comparison isochore clusters of 0–35 wt.% H_3BO_3 solutions having the same $T_{hom.}$. The detailed explanation is in the text.

H_2O within 500–720 °C. Crystallization of a water-saturated, B-, F-rich pegmatite melt would result in separation of an aqueous fluid phase (F_1) at given P_o and T_o. Such fluids are separated in a viscous medium of a residual melt as "bubbles" of different volumes and densities. The densities of the bubbles can be different due to many factors, e.g. variable composition of residual melts within the same body, time, P_o and T_o of fluid separation. The conservation of the residual melt and the released fluid F_1 by the early quartz–feldspar pegmatite minerals should be regarded as an initial stage of pocket formation. Further crystallization of the melt would bring an additional amount of fluid (F_2) into the fluid "bubble" and increase its density. Therefore, the internal fluid pressure would increase and reach a maximum at the solidus temperature of the residual melt (Fig. 12). In each pocket, ΔP depends on the initial temperature and pressure of their formation (T_o, P_o), the volume ratio of fluid (F_1) and residual melt, and the amount

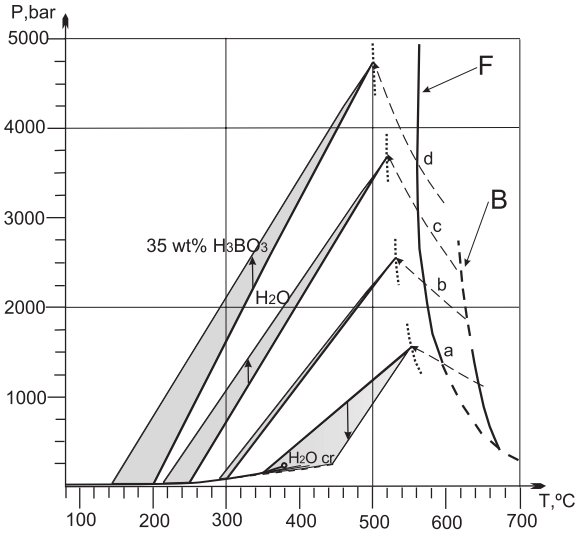

Fig. 12. Schematic P–T-paths of miarole-forming system isolated under different P–T-conditions in boron-rich pegmatite. Dashed lines show hypothetic P–T-paths of heterogeneous fluid + melt systems during crystallization of melt within 650–550 °C (a), 630–530 °C (b), 620–520 °C (c), 600–500 °C (d). P–T-paths follow isochores of aqueous fluids below the solidus of the residual melt. Shaded areas show isochores of 0–35 wt.% H_3BO_3 aqueous fluids derived from the melt at the same temperature. B—solidus of water-saturated haplogranite melt coexisting with 11 wt.% H_3BO_3 aqueous fluid by Manning and Pichavant (1983). F—solidus of water-saturated granite melt, containing 3 wt.% of F by Thomas et al. (1991).

and composition of additionally released fluid (F_2). Below the solidus of residual melt, the pressure in the cavities decreases along corresponding isochores and depends on H_3BO_3 content and the concentration of other solvents (Fig. 12). Data on FMI microthermometry suggest that solidus temperatures of the late melts of the Oktyabrskaya pegmatite are lower than those experimentally determined for water-saturated melts containing 3 wt.% of F (Thomas et al., 1991) and melts, coexisting with 11 wt.% H_3BO_3 aqueous fluid (Manning and Pichavant, 1983) (solidi are shown for reference in Fig. 12), although the studied melts have similar concentrations of B and F. This could be explained by a combined effect of B, F, H_2O and some rare elements on the crystallization of the latest melts.

Taking into consideration the above discussion one can expect that cavities with different internal pressures may form within one pegmatite body. A significant difference between pressures of neighboring pockets may increase the probability of pocket fracturing due to tectonics, intra-vein deformation, shrinkage strain, etc. Rapid fracturing of pockets may be like "a fluid explosion", which partly damages the pocket walls. Such "explosions" may damage druse material and form new fractures, which can open adjacent pockets and initiate boiling (heterogenization) and mixing of fluids from several pockets. The pocket fluids would fill these newly formed fractures and interact with the primary pegmatite matrix inducing the observed autometasomatic transformations. In a number of cases they form so-called primary–secondary pockets of complex morphology (Zagorsky et al., 1999b). Abrupt changes of composition, the aggregate state and fluid pressure favor dissolution, recrystallization and regeneration of different minerals, both in pockets and in the surrounding pegmatite matrix. This model is consistent with the mineralogical observations of various pegmatites made by many scientists worldwide and with available data on FI and MI (Foord, 1977; Foord et al., 1989; Zagorsky et al., 1999b).

The above arguments and interpretations do not take into consideration more compositionally complicated fluids, interaction of the fluid with pocket wall minerals and earlier pocket mineral assemblages, possible separation of gas phases, change of cavity volumes due to a crystal growth and other factors. However, the effect of such factors would obviously make the model more complicated and lead to more pronounced variations of

the fluid pressure in miarolitic cavities but would not change the main conclusions.

8. Conclusions

The results of the study of a miarolitic cavity of the Oktyabrskaya pegmatite reveal characteristic features of miarolitic pocket formation. The Oktyabrskaya pegmatite is a typical example of shallow-seated sub-rare-metal tourmaline-rich gem pegmatites of the Malkhan field. The formation of the pocket started at about 600 °C in a system consisting of two immiscible liquids: an aluminosilicate H_2O-, B-, F-bearing residual melt enriched in alkaline metals and rare granitophile elements and a boric acid aqueous fluid. Although the fluid dominated this system with respect to the melt, the latter played an important role in the formation of early pocket mineral parageneses. Nevertheless, in some parts of pegmatite bodies, the residual melts could have accumulated in amounts sufficient for the formation of near-pocket complexes with rare-metal mineralization, e.g. lepidolite, Li-tourmaline, petalite, pollucite, beryl and diverse tantaloniobates. The capability of residual melts to accumulate various rare elements suggests their importance in the processes of ore formation in pegmatites. The study of several hundred specimens of quartz, tourmaline, beryl and adularia from pockets and near-pocket assemblages of the pegmatites of the Malkhan field, Borshovochny range (East Transbaikalia), Middle Urals, Central and South-Western Pamirs, and Namibia revealed that similar MI usually occur at the base of pocket crystals. However, judging from the wide diversity of near-pocket and druse minerals, the compositions of the residual melts and fluids participating in their formation were greatly variable within the same pegmatite body. The study of such unusual melts, which are similar to the studied ones, is important for reconstructing the processes of mineral and ore formation at the final stages of magmatic crystallization in pegmatites and requires further thorough investigations.

Compositional heterogeneity of residual melts and associated fluids as well as differences in $P-T$-parameters of conservation of miarolitic fluid/melt system may result in significant variations of fluid pressure in the course of miarolitic pocket formation.

Acknowledgements

The authors thank Dr. F.G. Reyf from the Buryat Geological Institute SB RAS (Ulan-Ude, Russia) and two anonymous reviewers for thoughtful comments and remarks that helped to clarify many important points on the presentation of experimental data and discussion. This manuscript was significantly improved by Dr. J. Webster. The study benefited from the help of Dr. B.A. Kolesov from the Institute of Inorganic Chemistry SB RAS (Novosibirsk, Russia), who helped to obtain the majority of Raman spectroscopy data. Authors thank I.A. Madyukov from Novosibirsk State University (Novosibirsk, Russia), who performed microthermometric measurements. Authors are grateful to I.Y. Safonova for her help in improving the English of the manuscript. This study was supported by the Russian Foundation for Basic Research grants 01-05-64677, 03-05-64436, 04-05-64389, 04-05-64109, and by the United Institute of Geology, Geophysics and Mineralogy SB RAS, the young scientist grant (2000–2002). **[SG]**

References

Azizov, N.D., Akhundov, T.S., 1996. Thermal properties of the aqueous solutions of boric acid at 298–573 K. High Temp. 34 (5), 788–791.

Bakumenko, I.T., Konovalenko, S.I., 1988. Formation features of miarolitic pegmatites and their position among granitic pegmatites. In: Sobolev, N.V., Bakumenko, I.T. (Eds.), Thermobarogeochemical Studies of Mineral-Forming Processes. Nauka, Siberian Branch, Novosibirsk, pp. 123–135. In Russian.

Černý, P., 1992. Geochemical and petrogenetic features of mineralization in rare-element granitic pegmatites in light of current research. Appl. Geochem. 7 (5), 393–416.

Černý, P., 2000. Constitution, petrology, affiliations and categories of miarolitic pegmatites. Mem. Soc. Ital. Sci. Nat. Mus. Civ. Stor. Nat. Milano 30, 5–12.

Di Giacomo, G., Brandani, P., Brandani, V., Del Re, G., 1993. Solubility of boric acid in aqueous solutions of chloride salts. Desalination 91 (1), 21–23.

Ermakov, N.P., 1972. Geochemical Systems of Inclusions in Minerals Nedra, Moscow. 375 pp. In Russian.

Fersman, A.E., 1960. Selected Works, vol. 6. Academy of Sciences of USSR, Moscow, pp. 148–250. In Russian.

Foord, E.E., 1977. Famous mineral localities: the Himalaya dike system, Mesa Grande district, San Diego county, California. Mineral. Rec. 6, 461–474.

Foord, E.E., Spaulding Jr., L.B., Mason, R.A., Martin, R.B. 1989. Mineralogy and paragenesis of the Little Tree mine pegmatites,

Ramona district, San Diego, California. Mineral. Rec. 20, 101–127.

Ginzburg, A.I., Rodionov, G.G., 1960. About depths of pegmatite formation. Geol. Ore Depos. 1, 45–54 (in Russian).

Ihinger, P.D., Hervig, R.L., McMillan, P.F., 1994. Analytical methods for volatiles in magmas. In: Carroll, M.R., Holloway, J.R. (Eds.), Volatiles in Magmas. Rev. Miner. 30, pp. 67–121.

Kalyuzhnyi, V.A., 1958. Improved thermal microscopic cell for analysis of gas–liquid inclusions. Tr. Vses. Naucno-Issled. Inst. Pézoopt. Miner. Syra 2 (2), 43–47 (in Russian).

Karpov, I.K., Chudnenko, K.V., Kulik, D.A., 1997. Modeling chemical mass-transfer in geochemical processes: thermodynamic relations, conditions of equilibria and numerical algorithms. Am. J. Sci. 297, 767–806.

Kovalenko, V.I., Tsareva, G.M., Naumov, V.B., Hervig, R.L., Newman, S., 1996. Magma of pegmatites from Volhynia—composition and crystallization parameters determined by magmatic inclusion studies. Petrology 4, 277–290.

Kosukhin, O.N., Bakumenko, I.T., Chupin, V.P., 1984. Magmatic Stage of Granitic Pegmatite Formation Nauka, Novosibirsk. 136 pp. In Russian.

London, D., 1986. Formation of tourmaline-rich gem pockets in miarolitic pegmatites. Am. Mineral. 71, 396–405.

London, D., 1999. Stability of tourmaline in peraluminous granite systems: the boron cycle from anatexis to hydrothermal aureoles. Eur. J. Mineral. 11 (2), 253–262.

Manning, D.A.C., Pichavant, M., 1983. The role of fluorine and boron in the generation of granitic melts. In: Al-herlon, M.P., Gribble, C.D. (Eds.), Migmatites, Melting and Metamorphism. Shiva Publ., Cheshire, U.K., pp. 94–109.

Manning, D.A.C., Martin, J.S., Pichavant, M., Henderson, C.M.B., 1984. The effect of F, B and Li on melt structures in the granite system: Different mechanisms? In: Henderson, C.M.B. (Ed.), Progress in Experimental Petrology. Nat. Env. Res. Council Publ. Ser. D 25, pp. 36–41.

Mikhailov, M.Y., Shatsky, V.S., 1975. Sillite heater for high-temperature heating stage. In: Sobolev, V.S. (Ed.), Mineralogy of Endogenous Formations (By Inclusions in Minerals). Nauka, Novosibirsk, pp. 109–110. In Russian.

Morgan, G.B., 1991. Studies pertaining to the role of boron in granitic magmas. Compass Sigma Gamma Epsil. 68 (4), 233–249.

Morgan, G.B., London, D., 1996. Optimizing the electron microprobe analysis of hydrous alkali aluminosilicate glasses. Am. Mineral. 81, 1176–1185.

Naumov, V.B., 1982. The use of methods of thermobarogeochemistry in the prospecting and study of ore deposits. In: Laverov, N.P. (Ed.), The Use of Methods of Thermobarogeochemistry in the Prospecting and Study of Ore Deposits. Nedra, Moscow, pp. 85–94. In Russian.

NIST-JANAF, 1998. Thermochemical tables, fourth edition. J. Phys. Chem. Ref. Data, Monogr. 9, 1951 pp.

Palkin, A.P., Goloschapov, M.V., 1939. Solubility in the system I. $Na_2SO_4–H_3BO_3–H_2O$ II. $NaCl–H_3BO_3–H_2O$. Tr. Voronez. Gos. Univ. 11 (1), 7–23 (in Russian).

Peretyazhko, I.S., Zagorsky, V.Ye., 2002. The influence of H_3BO_3 on fluid pressure in granitic pegmatite miaroles: a computation of isochors and the density of boric solutions. Dokl. Earth Sci. 383A (3), 340–345.

Peretyazhko, I.S., Zagorsky, V.Ye., Prokof'ev, V.Yu., Smirnov, S.Z., 1999. Boric acid as the most typical component of fluid inclusions in minerals from tourmaline-bearing and topaz–beryl miarolitic pegmatites. Can. Miner. 37, 823–825.

Peretyazhko, I.S., Prokofiev, V.Yu., Zagorsky, V.Ye., Smirnov, S.Z., 2000. Role of boric acids in the formation of pegmatite and hydrothermal minerals: Petrologic consequences of sassolite (H_3BO_3) discovery in fluid inclusions. Petrology 8, 214–237.

Peretyazhko, I.S., Zagorsky, V.Ye., Smirnov, S.Z., Mikhailov, M.Yu., Prokofiev, V.Yu., Madyukov, I.A., 2002a. The model of pocket formation in boron-rich granitic pegmatites. Goldschmidt conference abstracts. Geochim. Cosmochim. Acta 66 (15A), 590.

Peretyazhko, I.S., Zagorsky, V.Ye., Smirnov, S.Z., Mikhailov, M.Yu., Prokofiev, V.Yu., 2002b. Processes of miarole formation in the course of boron and water-rich melt crystallization in granitic pegmatites. Abstracts of Conf. "Geology, Geochemistry and Geophysics at the XX and XXI Century Edge (RFBR in Asian region)". Irkutsk, Russia, pp. 373–375. In Russian.

Pichavant, M., 1987. Effects of B and H_2O on liquidus phase relation in the haplogranite system at 1 kbar. Am. Mineral. 72, 1056–1070.

Pokrovski, G.S., Schott, J., Sergeev, A.S., 1995. Experimental determination of the stability constants of $NaSO_4^-$ and $NaB(OH)_4^0$ in hydrothermal solutions using a new high-temperature sodium-selective glass electrode—Implications for boron isotopic fractionation. Chem. Geol. 124, 253–265.

Roedder, E., 1984. Fluid Inclusions. Reviews in Mineralogy, vol. 12. Mineral. Soc. Am., Washington, DC. 644 pp.

Ryss, I.G., 1956. The Chemistry of Fluorine and its Inorganic Compounds Gos. Izdatelstvo Khim. Lit., Moscow. 718 pp. In Russian.

Ryss, I.G., Slutskaya, M.M., Vitukhnovskaya, B.S., 1952. Equilibrium of the system sodium fluoride–boric acid–water at 25 °C. Zhurnal Prikladnoi Khimii 25, 148–153 (in Russian).

Samoilovich, L.A., 1969. Relationship Between Pressure and Density of Water–Salt Solutions: Handbook VNIISIMS, Moscow. 47 pp. In Russian.

Simonov, V.A., 1993. Petrogenesis of Ophiolites Nauka, Novosibirsk. 247 pp. In Russian.

Smirnov, S.Z., Peretyazhko, I.S., Prokof'ev, V.Yu., Zagorsky, V.Ye., Shebanin, A.P., 2000. The first finding of sassolite (H_3BO_3) in fluid inclusions in minerals. Russ. Geol. Geophys. 41 (2), 193–205.

Smirnov, S.Z., Peretyazhko, I.S., Zagorsky, V.Ye., Mikhailov, M.Yu., 2003. The evidence of unusual melts from melt inclusions in pocket quartz of the Oktyabrskaya mine, Malkhan Ridge, Central Transbaikalia. In: Degi, J., Szabo, C.S. (Eds.), ECROFI VII Abstracts. Acta Mineral.-Petrogr., Abstr. Ser. 2, pp. 188–189.

Sobolev, A.V., 1996. Melt inclusions in minerals as a source of principle petrological information. Petrology 4, 209–220.

Thomas, R., 2002. Determination of the H_3BO_3 concentration in fluid and melt inclusions in granite pegmatites by laser Raman microprobe spectroscopy. Am. Mineral. 87, 56–68.

Thomas, R., Förster, H.-J., Tischendorf, G., 1991. PTX-signatures of Hercynian ore-producing granites, Erzgebirge, Germany. In: Pagel, M., Leroy, J.L. (Eds.), Source, Transport and Deposition

of Metals. Proc. of 25 years SGA aniv. Meeting, Nancy. A.A. Balkema, Rotterdam, pp. 231–234.

Thomas, R., Webster, J.D., Heinrich, W., 2000. Melt inclusions in pegmatite quartz: complete miscibility between silicate melts and hydrous fluids at low pressure. Contrib. Mineral. Petrol. 139, 394–401.

Thomas, R., Förster, H.-J., Heinrich, W., 2003. The behaviour of boron in peraluminous granite–pegmatite system and associated hydrothermal solutions: a melt and fluid-inclusion study. Contrib. Mineral. Petrol. 144, 457–472.

Veksler, I.V., Thomas, R., Schmidt, C., 2002. Experimental evidence of three coexisting immiscible fluids in synthetic granitic pegmatite. Am. Mineral. 87, 775–779.

Zagorsky, V.Ye., Peretyazhko, I.S., 1992a. Pegmatites with Precious Stones of the Central Transbaikalia Nauka, Novosibirsk 224 pp. In Russian.

Zagorsky, V.Ye., Peretyazhko, I.S., 1992b. Types and average composition of miarolitic pegmatite of Malkhan ridge. Geol. Geofiz. 1, 87–98 (in Russian).

Zagorsky, V.Ye., Shmakin, B.M., 1987. Principles of classification of granitic pegmatites. In: Shmakin, B.M. (Ed.), Modern Problems of Theoretical and Applied Geochemistry. Nauka Press, Novosibirsk, pp. 57–63. In Russian.

Zagorsky, V.Ye., Shmakin, B.M., 1997. Pegmatitic deposits of gemstones as miarolitic facies of pegmatites of different formationsAbstracts of III Intern. Conf. "New ideas in earth science", Moscow, vol. 2. Publ. House MSGPU, p. 61.

Zagorsky, V.Ye., Makagon, V.M., Shmakin, B.M., 1999a. The systematics of granitic pegmatites. Can. Miner. 37, 800–802.

Zagorsky, V.Ye., Peretyazhko, I.S., Shmakin, B.M., 1999b. Granitic Pegmatites. Miarolitic Pegmatites, vol. 3. Nauka, Novosibirsk. 485 pp. In Russian.

Zagorsky, V.Ye., Makagon, V.M., Shmakin, B.M., 2003. Systematics of granitic pegmatites. Russ. Geol. Geophys. 4 (5), 422–435.

Zhdanoviskii, B.A., Likhovskaya, E.I., Shleymovich, R.E., 1975. Handbook on Solubility in Multicomponent Water–Salt System Khimiya, Leningrad. 1063 pp. In Russian.